





Optimal geometries for low-resistance viscous electron flow

J. Estrada-Álvarez ^{*}, F. Bermúdez-Mendoza ^{*}, F. Domínguez-Adame , and E. Díaz [†]
GISC, Departamento de Física de Materiales, Universidad Complutense, E-28040 Madrid, Spain

 (Received 12 December 2024; revised 9 January 2025; accepted 15 January 2025; published 3 February 2025)

This work explores the impact of geometry on viscous electron flow in graphene channels. We demonstrate that structural modifications of the material edges distinctly influence its electrical resistance. As a general trend, we observe that softening the edges reduces the resistance in both the hydrodynamic and the ballistic regimes. Our simulations are based on a two-dimensional hydrodynamic model, which is compared with those obtained by the Boltzmann transport equation in some representative cases. In both formalisms, the scattering length due to electron-electron collisions and due to momentum-relaxing collisions of electrons with impurities and phonons are taken into account. A minimization algorithm was employed to optimize the channel geometry of the minimal resistance. Our findings emphasize the critical role of the channel geometry in graphene, presenting significant implications for the design of advanced electronic devices based on two-dimensional materials.

DOI: [10.1103/PhysRevB.111.075401](https://doi.org/10.1103/PhysRevB.111.075401)

I. INTRODUCTION

The future of electronics relies on developing miniaturized circuits with low energy costs. Conventional silicon-based technology shall reach its physical limits, so the research on new two-dimensional (2D) devices turns promising [1]. Two-dimensional materials also exhibit novel transport properties, such as hydrodynamic transport, where the electrons behave like a fluid. While electron transport in metals is often determined by collisions against defects and phonons, recent research in two-dimensional materials highlights the significance of electron-electron collisions as a source of hydrodynamic effects [2–6]. Experiments in graphene, gallium arsenide heterostructures [7], Weyl semimetals [8–11], and PdCoO₂ have unveiled [12,13] fascinating phenomena that challenge our common expectations about electron behavior in solids. This encompasses the Poiseuille flow [14,15] or the formation of whirlpools in symmetry-broken devices [16–19], and it also features potential high-frequency applications [20–24].

However, one of the most salient features of viscous electron flow, which brings us back to the problem of energy dissipation [25,26], is the so-called superballistic conduction [27–33]. Originally suggested by Gurzhi [34,35], an increase in temperature favors collective electron flow, decreasing the resistance below the ballistic limit, a very convenient property to reduce device energy dissipation [36]. The application of a high current also attains a similar decrease [37,38]. A careful geometrical design of the device is proven to enhance its collective transport properties [14]. This underscores the key role of the geometry in hydrodynamic transport [39], and showcases the potential to design graphene-based devices with tailored electronic transport properties [28].

In this work, we explore the implications of the device geometry on electron flow in graphene by examining

geometric modifications in constrictions and bent channels. The optimized devices will present minimal values of electrical resistance. We find that a strategic reduction or extension of the graphene channel led to lower resistances, depending on the transport regime [2,6]. This approach promises to unlock properties of 2D materials like graphene to achieve low-electrical-resistance devices.

II. MODEL

A. Boltzmann transport equation

In order to provide an accurate description of electronic transport in engineered graphene devices, we will deal with two different theoretical formalisms. Let us first consider the steady-state Boltzmann transport equation to describe the dynamics of semiclassical electrons in a 2D system [40,41]. In electron hydrodynamics the explored devices have many transmission channels, so quantization effects are negligible, and electrons can be monitored by a well-defined position vector $\mathbf{r} = (x, y)$ and a wave vector $\mathbf{k} = (k_x, k_y)$, such that their distribution function $f(\mathbf{r}, \mathbf{k})$ obeys [6,32,33,41–44]

$$\frac{v}{k} \mathbf{k} \cdot \nabla_{\mathbf{r}} f + \frac{e}{\hbar} \nabla V \cdot \nabla_{\mathbf{k}} f = \Gamma[f]. \quad (1)$$

Electrons experience a force due to the electric potential $V(\mathbf{r})$, and $\Gamma[f]$ is the collision operator, including the sources of electron scattering. Under Callaway's ansatz [38,45], the collision term splits as

$$\Gamma[f] = -v_{\text{F}}[(f - f^{mr})/l_{mr} + (f - f^{ee})/l_{ee}], \quad (2)$$

where l_{mr} is the mean free path due to momentum-relaxing collisions with impurities and phonons toward the equilibrium distribution f^{mr} , and l_{ee} accounts for electron-electron collisions with other electrons toward the local distribution f^{ee} shifted by the electron drift velocity. The fluid viscosity, which will appear explicitly in the hydrodynamic model, derives from these collisions [see Eq. (6) below]. We use the hydrodynamic electron dynamics instead of the

^{*}These authors contributed equally to this work.

[†]Contact author: elenadg@fis.ucm.es

tomographic correction [46–48], which would be less noticeable at moderate temperatures and would otherwise add additional parameters to the model. Here, v_F and k_F are the Fermi velocity and the Fermi wave number, respectively. We assume that a gate voltage sets a uniform electron density in the device under study. Therefore, f^{mr} turns out to be independent of \mathbf{r} . After integrating Eq. (1) over k , we get

$$\hat{\mathbf{n}}(\theta) \cdot \nabla_{\mathbf{r}} \left(g - \frac{eV}{\hbar k_F} \right) + \frac{g}{l_{mr}} + \frac{g - g^{ee}}{l_{ee}} = 0, \quad (3)$$

with $\hat{\mathbf{n}}(\theta) = (\cos \theta, \sin \theta)$. For brevity, we have defined

$$g^{ee}(\mathbf{r}, \theta) = \frac{v_F}{k_F} \int_0^\infty (f^{ee} - f^e) dk \simeq u_x \cos \theta + u_y \sin \theta, \\ g(\mathbf{r}, \theta) = \frac{v_F}{k_F} \int_0^\infty (f - f^{mr}) dk, \quad (4)$$

where u_x and u_y are the components of the drift velocity $\mathbf{u}(\mathbf{r}) = (1/\pi) \int_0^{2\pi} g(\mathbf{r}, \theta) \hat{\mathbf{n}}(\theta) d\theta$. The Boltzmann model is valid for hydrodynamic, diffusive, and ballistic electron transport [6].

B. Navier-Stokes equation

The second formalism can be derived as a hydrodynamic model [16,18,49,50] for the drift velocity \mathbf{u} , recasting Eq. (3) as [6]

$$\nabla \cdot \mathbf{u} = 0, \quad (5a)$$

$$-\nu \nabla^2 \mathbf{u} + \frac{v_F}{l_{mr}} \mathbf{u} = \frac{e}{m} \nabla V, \quad (5b)$$

which resemble the continuity equation and the Navier-Stokes equation for classical fluids [2,3,14,16]. The viscosity ν is defined as follows:

$$\nu \equiv \frac{v_F l_{mr} l_{ee}}{4(l_{mr} + l_{ee})}. \quad (6)$$

Hence, favoring electron-electron collisions diminishes the viscosity and its associated dissipation. Notice that Eq. (5b) has a dissipative term in \mathbf{u} arising from non-conserving-momentum collisions ($l_{mr} < \infty$), as expected in condensed matter systems.

In both models, we consider two types of boundary scattering mechanisms [51]. First, unless stated otherwise, we consider a perfectly specular edge with no roughness, where incident electrons undergo specular reflection. This type of edge is consistent with previous experiments in graphene [28]. For completeness, we analyze the opposite case, a rough diffusive boundary where incident electrons are scattered in all directions regardless of their angle of incidence. We describe the equivalence between the boundary conditions for both formalisms in Appendix A [6]. Simulations are performed using the finite elements method described in Appendix B to determine the velocity field \mathbf{u} and the resistance R .

Our approach follows the technological perspective, where devices are supposed to operate at a given temperature, with a particular l_{mr} and l_{ee} . For clarity, we instead perform our analysis in terms of the normalized electron-electron and momentum-relaxing scattering rates, $\gamma_{ee} = W/l_{ee}$ and

$\gamma_{mr} = W/l_{mr}$, where W is the scale length of the device. Thus, we explore the effects of the device geometry on the electrical performance, with the ultimate goal of identifying the configuration of minimal resistance for a given temperature R_0 [14]. We will compare R_0 with a reference device of sharp corners of resistance R_\perp by way of

$$\Delta R = \frac{R_\perp - R_0}{R_\perp}. \quad (7)$$

In this investigation, we want to explore the effects of optimized edge engineering on graphene devices' electrical performance. Therefore, we propose two different typical geometries to exemplify our findings: (1) a 2D graphene elbow channel and (2) a graphene constriction.

III. 2D ELBOW CHANNEL

First, we will focus on the study of the 2D elbow channel. The geometry depicted in Fig. 1(a) represents a 2D elbow graphene channel of width W . Bending the profile is particularly significant because it might reduce undesirable scattering events at the boundaries when properly designed. Therefore, in our study, we take as a reference case a graphene elbow of a perfect 90° angle, where the electrical resistance R_\perp is expected to be high. Let us first study the configuration of minimal resistance by analyzing the Boltzmann equation results in comparison with those obtained by the Navier-Stokes model. Notice that the computational cost of the Boltzmann model forces us to design the geometries using only three points $\vec{G} = \{H_1, G_1, G_2\}$, see Fig. 1(a). The color map of Fig. 1(b) represents the resistance as a function of \vec{G} , which shows that it is minimal at the white dot. For a given potential drop, a minimum in the resistance corresponds to a maximum in the current flow, which is the magnitude typically studied in conventional fluids. The formalism based on the Navier-Stokes equation allows a much more detailed design of the elbow corner. In our simulations, we tested that by varying at least a vector of points $\vec{G} = \{H_1, \dots, H_5, G_1, \dots, G_5\}$, the optimal geometry is already stable. Figures 1(c) and 1(d) illustrate the voltage drop across the optimized channel with minimal resistance R_0 , for $\gamma_{ee} = 1$ and $\gamma_{mr} = 1/3$, similar to the ratios obtained for a graphene device of $W \sim 300$ nm at carrier density $n \sim 10^{12} \text{ cm}^{-2}$ and room temperature [16,18]. We assume perfect specular boundaries for both models. For comparison, the black dashed line represents the reference 90° corner with resistance R_\perp . Both optimized geometries feature a smoother bent, reducing boundary scattering, allowing for a more uniform collective flow and reducing the resistance. In such a case, we evaluate that the geometry optimization process leads to a relative change of the resistance ΔR of 31% with the Boltzmann model and 39% with the smoother edge simulated with the Navier model. Such a reduction of the electrical resistance is consistent with the fact that sharp edges cause additional boundary scattering: smoother geometries are necessary to improve flow efficiency in constrained geometries.

Now, we extend our analysis to different values of γ_{ee} and γ_{mr} to account for different transport regimes. For every considered case, we performed the geometry optimization and evaluated the minimal resistance compared to the

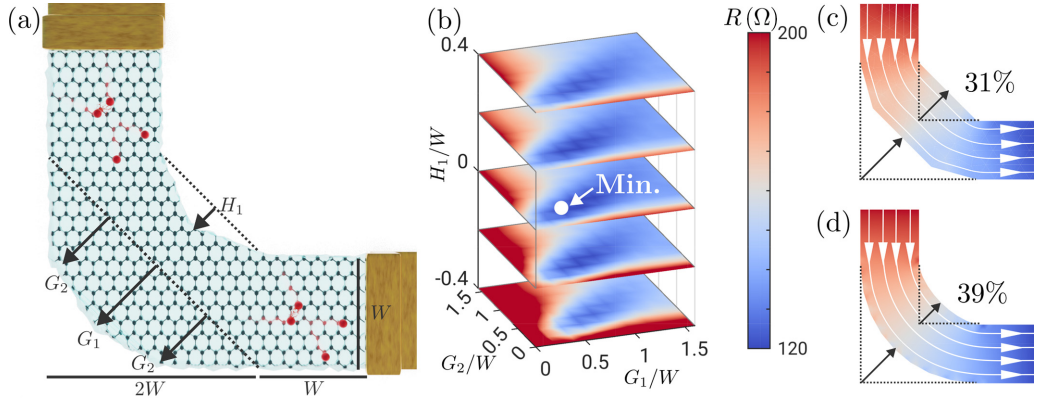


FIG. 1. (a) The schematic represents a graphene channel of width W with an elbow. The quadrant of size $2W \times 2W$ where the bend occurs is the varying region for the optimization process. The dashed black line represents the initial geometry from which variations are considered by defining the sampling points as $\vec{G} = \{H_1, G_1, G_2\}$. (b) Resistance obtained by Boltzmann equation with specular boundaries when $\gamma_{ee} = 1$ and $\gamma_{mr} = 1/3$ in every geometry defined by \vec{G} . A stable minimum resistance is found for the parameters indicated by the white dot. (c) and (d) Voltage distribution across the optimal graphene elbow with the minimum resistance obtained by the Boltzmann and Navier equations, respectively. The color represents the voltages, and the black dashed line corresponds to the reference 90° corner.

reference case. In Fig. 2(a), we show the optimized elbow obtained within the Boltzmann (colored region) and the Navier models (black solid line) formalism. We demonstrate that smooth boundaries reduce the system's resistance in all cases. However, depending on the particular scattering rates, the optimized geometry might also widen the bend region, mainly when $\gamma_{mr} \geq 1$ and the transport is mainly diffusive. By considering the Navier equation, the minimal electrical resistance R_0 and the resistance reduction ΔR are presented in Figs. 2(b) and 2(c) as a function of the parameters γ_{mr} and γ_{ee} for specular boundaries. Notice that the bottom shaded region with $\gamma_{mr} \leq 0.5$ and $\gamma_{ee} \leq 1.0$ has not been considered since for such parameters, ballistic effects are relevant, and therefore, the Navier model is not expected to be accurate [6]. As shown, by increasing γ_{ee} , the reduction of the

resistance by the optimal geometry is weaker, mostly if γ_{mr} is also significant. This is consistent with the fact that as γ_{mr} increases, scattering due to impurities or phonons is dominant, and the influence of boundary scattering diminishes. Therefore, the effect of the particular geometry is not that significant. Still, if γ_{ee} is high enough ($\gamma_{ee} > 1$) and γ_{mr} is reduced, as it happens when we miniaturize the electronic devices, electron transport is primarily dictated by electron-electron interactions, and we demonstrate that the geometry optimization may lead to a reduction of the resistance near 40%.

IV. GRAPHENE CONSTRICTION

In the following, we will deal with another relevant geometry considered in transport experiments: a graphene constriction. The latter is defined by fixing the width and length of the constriction to W , which are the width and total length of the channel $3W$ and $6W$, respectively. By setting the origin of the coordinate system at the center of the constriction, let us confine the geometry optimization in the first Cartesian quadrant and reproduce the process symmetrically across the remaining ones. We then dynamically varied the geometry by strategically positioning a sample of points between $[W/2, W/2]$ and $[2W, 3W/2]$. As considered in the previous section, the Boltzmann formalism is used under a simplified process where only two points $\vec{G} = \{G_1, G_2\}$ are considered in the varying region [see Fig. 3(a)]. At the same time, for the Navier equation we take a higher number of sampling points to soften the obtained profile $\vec{G} = \{G_1, \dots, G_4\}$. For clarity, Fig. 3(b) represents a color map of the resistance obtained with the Boltzmann equation for a set of sampling points where a stable minimum value arises. In order to evaluate the resistance reduction due to the geometry optimization, we now consider as a reference case a square constriction with resistance R_\perp , see dashed profiles in Figs. 3(c) and 3(d). They illustrate the voltage drop across the optimized constriction with minimal resistance R_0 , when $\gamma_{ee} = 2$ and $\gamma_{mr} = 1/3$ for the Boltzmann ($\Delta R = 9\%$)

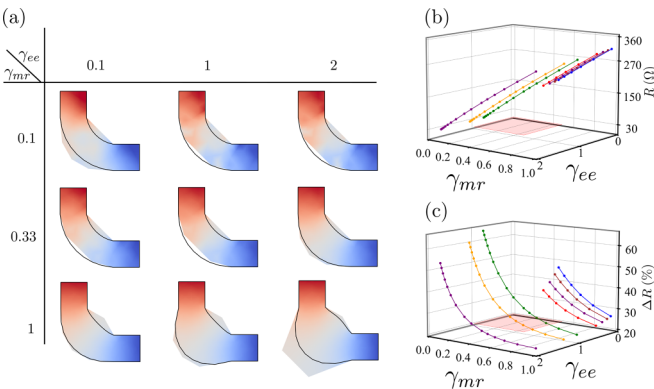


FIG. 2. (a) Optimized geometries with minimal resistance calculated by Boltzmann (colored region) and Navier (solid black line) formalisms for different rates γ_{mr} and γ_{ee} . (b) Minimal resistance obtained with Navier equation and specular boundaries as a function of the parameters γ_{mr} and γ_{ee} . The red-shaded region represents the parameter space where the Navier model does not provide reliable results. (c) Relative change in resistance ΔR between the one of the 90° corner R_\perp (non-optimized-geometry) and the one of the optimized geometry R_0 shown in (b).

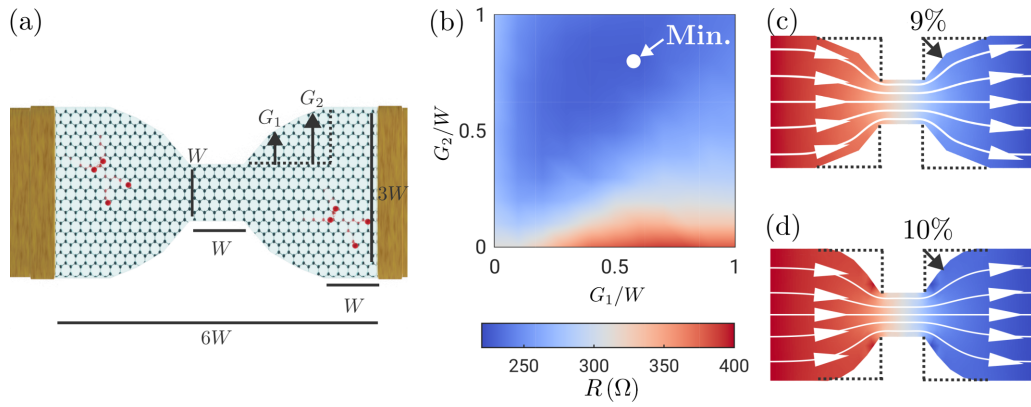


FIG. 3. (a) Schematic representation of a graphene channel of width $3W$ with a constriction of width W . The geometry variation is performed by dynamically positioning a sample of points between $[W/2, W/2]$ and $[2W, 3W/2]$, with respect to the center of the constriction. The dashed black line represents the initial geometry from which variations are considered by defining different sampling points as $\vec{G} = \{G_1, G_2\}$ in the Boltzmann formalism. For the Navier model, a larger number of points is considered (not shown in the plot). (b) Resistance obtained by the Boltzmann model with specular boundaries when $\gamma_{ee} = 2$ and $\gamma_{mr} = 1/3$ in every geometry defined by \vec{G} . A stable minimum resistance is found for the parameters indicated by the white dot. (c) and (d) Voltage distribution across the optimal graphene constriction with the minimum resistance obtained by the Boltzmann equation for \vec{G} marked in (b) and for the Navier model, respectively. The color gradient represents values from lower voltages (blue) to higher ones (red), and the black dashed line is the reference square constriction.

and Navier models ($\Delta R = 10\%$) with specular boundaries, respectively. Both optimized geometries feature a smoother curved profile that is consistent with the results of the previous section. Such a reduction, although lower than the one found in the elbow channel, is still relevant for applications, and it can be enhanced with a proper choice of parameters γ_{ee} and γ_{mr} .

Now, let us analyze the reduction of constriction resistance after optimizing different transport parameters. Our results are

summarized in Fig. 4. Moreover, in this section, we want to discuss the effect of the considered boundary, namely, rough or specular. In Fig. 4(a) we show the optimal geometry of minimal resistance obtained with the Boltzmann (colored region) and Navier models (solid line) for a particular set of values γ_{ee} and γ_{mr} . In addition, on each panel, the right (left) half corresponds to the solution with rough (specular) edges as indicated. Given the results shown in Fig. 4, it is clear that the main conclusion of the previous section

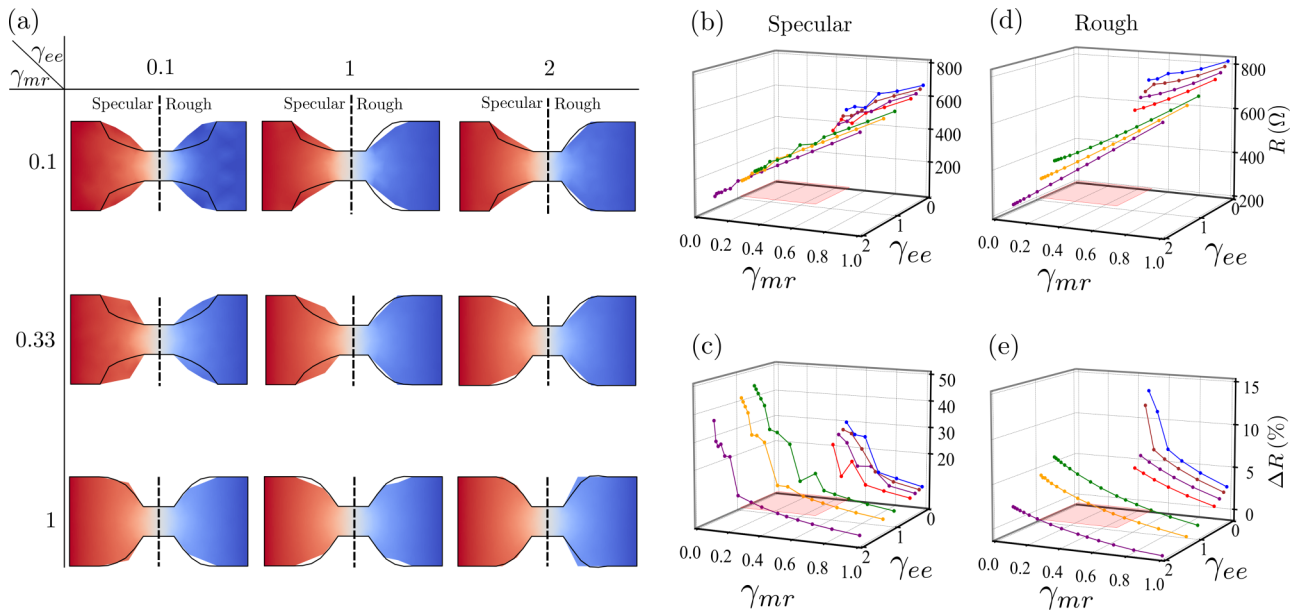


FIG. 4. (a) Optimized geometries with minimal resistance calculated by Boltzmann (colored region) and Navier models (solid black line) formalisms for different rates γ_{mr} and γ_{ee} . In every panel, the right (left) half corresponds to the solution with rough (specular) edges as indicated. (b) Minimal resistance obtained with Navier equation and specular boundaries as a function of the parameters γ_{mr} and γ_{ee} . The red-shaded region represents the parameter space where the Navier model does not provide reliable results. (c) Relative change in resistance ΔR between the one of the square constriction R_{\perp} (non-optimized-geometry) and the one of the optimized geometry R_0 shown in (b). (d) and (e) Same as in (b) and (c) but considering rough boundaries.

remains: the optimal geometry of minimal resistance arises after smoothing the edge curvature. Particularly for the case of the constrictions, we observe more disparities between the Boltzmann and Navier solutions, especially when $\gamma_{ee} < 1$ and $\gamma_{mr} < 1$. Still, this is consistent with the fact that for such rates, ballistic effects are relevant, and the validity of the Navier model is compromised. Regarding the choice of the type of edge scattering, we observe that the profile smoothing is still revealed as the way to minimize resistance in both cases, rough or specular boundaries. However, the particular sign of the curvature of the constricted region might depend on the scattering at the boundaries (see, for example, the case $\gamma_{ee} = 2$ and $\gamma_{mr} = 0.1$). Figures 4(b)–4(e) also represent the minimal resistance and its reduction compared to a square constriction calculated with the Navier model for specular or rough edges. The dependency of the minimal resistance of the constriction with the scattering rates is the same as found in the elbow channel; see Fig. 2(b). Although there is an overall decrease in the resistance reduction obtained for the constriction geometry, especially for rough edges, if γ_{ee} is high enough ($\gamma_{ee} > 1$) and γ_{mr} is reduced, ΔR can reach significant values near 25% for specular boundaries.

V. CONCLUSIONS

This work highlights geometry engineering as a crucial tool to exploit hydrodynamic signatures in 2D devices. Our findings are pivotal for designing less resistive electronic devices and underscore the importance of geometric optimization and computational methods in device design. We have demonstrated that a careful modification of a graphene channel geometry, mostly by smoothing its curvature, reduces the dissipative boundary scattering. Two different formalisms have confirmed our results: (1) a general Boltzmann transport equation and (2) a fully hydrodynamic model based on the Navier-Stokes equation. We also considered different scattering rates for the electron-electron interactions and the momentum-relaxing processes. Therefore, we were able to establish that our conclusions are expected to be valid when the electron flow is mostly collective, i.e., if γ_{ee} is high enough ($\gamma_{ee} > 1$) and γ_{mr} is reduced ($\gamma_{mr} < 1/3$). We demonstrate an average reduction in the electrical resistance of 40% in a 2D graphene elbow and of 25% in a graphene constriction when properly smoothing its curvature in comparison with their analog defined with right angles. In addition, we observe that the uncontrolled roughness of the edges is a detrimental factor in reducing the electrical resistance with geometry optimization. Therefore, specular edges [51,52] are desirable. For a default geometry, electron-electron collisions have been shown to reduce the electrical resistance for a given geometry [36]. However, the resistance could be further reduced by choosing the optimal geometry, following the optimization process in our paper. Moreover, even when a circuit has to operate at a given temperature, the geometry is still a feasible route to optimize its electrical performance. Our results allow for improved functionality and efficiency of graphene-based electronic devices, enabling the development of high-performance materials with significantly optimized electronic properties.

ACKNOWLEDGMENTS

This work was supported by the “(MAD2D-CM)-UCM” project funded by Comunidad de Madrid; by the Recovery, Transformation and Resilience Plan; and by NextGenerationEU from the European Union and Agencia Estatal de Investigación of Spain (Grant No. PID2022-136285NB-C31). J.E. acknowledges support from the Spanish Ministerio de Ciencia, Innovación y Universidades (Grant No. FPU22/01039).

DATA AVAILABILITY

The data that support the findings of this article are not publicly available upon publication because it is not technically feasible and/or the cost of preparing, depositing, and hosting the data would be prohibitive within the terms of this research project. The data are available from the authors upon reasonable request.

APPENDIX A: BOUNDARY CONDITIONS

The two common boundaries considered in the literature [51] are the rough edges that assume

$$g(\theta) = 0 \quad (\text{A1})$$

for all reflected electrons but not for the incident ones and the partially specular edges that read

$$g(\theta) = g(-\theta) + d \sin \theta \times \left[g(-\theta) - \frac{2}{\pi} \sin \theta \int_0^\pi \sin^2 \theta' g(-\theta') d\theta' \right], \quad (\text{A2})$$

where $0 < \theta < \pi$ are the reflected electrons and $-\pi < \theta < 0$ are the incident ones. For the sake of simplicity, we wrote the boundary condition for an edge parallel to $\theta = 0$. Here, $d \equiv \sqrt{\pi} h^2 h' k_F^3 \lesssim 1$ is the dispersion coefficient, with h the edge's bumps mean height and h' its correlation length. In particular, the perfectly specular boundary conditions reads

$$g(\theta) = g(-\theta). \quad (\text{A3})$$

When defining boundaries in the Navier equation, we use the additional condition $\partial_x u_y = -u_y/\xi$, where $\xi = 3\pi v/4v_F$ is known as the slip length [6]. The exact expressions for the Navier-Stokes equation conditions in terms of the so-called slip length ξ [51,53] are reported in Ref. [6] and result in the following definitions:

$$\xi = \begin{cases} \frac{3\pi}{4} \frac{v}{v_F}, & \text{rough edge,} \\ 8\left(\frac{1}{d} - \frac{2}{3\pi}\right) \frac{v}{v_F}, & \text{specular edge.} \end{cases} \quad (\text{A4})$$

Mainly, when $d = 0$, the edge has no roughness but is perfectly specular and $\xi \rightarrow \infty$, which is the case considered in our study (see Ref. [6] for further details of the theoretical model).

APPENDIX B: NUMERICAL METHODS

We use a conformal Galerkin finite element method to solve both transport models [6,54]. We approximate the

solution to the Boltzmann equation as

$$g(\mathbf{r}, \theta) = \sum_{n=1}^N \sum_{m=1}^M g_{nm} \phi_n(\mathbf{r}) \varphi_m(\theta). \quad (\text{B1})$$

The spatial elements $\{\phi_n\}_{n=1}^N$ are the set of tent functions and their bubbles defined on a triangular mesh. The points that define a geometry act as vertices of a Delaunay triangulation process, ensuring that the mesh is sensitive to the features of the graphene channel. The Delaunay criterion results in well-conditioned, near-equilateral triangles. The mesh is refined iteratively [55,56], which avoids slender elements and improves computational performance [57]. This process mitigates the impact of the numerical errors in the optimization process, especially when comparing similar geometries. We achieve convergence by setting the maximum size of the triangles $h < 0.2W$ for the elbow geometry and $h < 0.4W$ for the constriction, which yields $N \sim 10^3$ spatial nodes. We also write the solution using angular elements $\{\varphi_m\}_{m=1}^M$, which are the tent functions defined on the periodic $[0, 2\pi)$ interval, and we take $M = 16$ to achieve convergence.

We write the weak formulation of Eq. (3), substitute Eq. (B1), and solve the resulting linear system using an iterative least-square method in MATLAB. At the edges, we impose the boundary condition in Eqs. (A1) or (A2) for reflected electrons. We set a constant density of carriers, and we impose periodic boundary conditions along the longitudinal direction to determine the g distribution at the limits of the simulated cell. We find similar results for a larger periodic cell, indicating that the periodic boundary conditions do not significantly affect the results. Once we determine $g(\mathbf{r}, \theta)$ and the potential $V(\mathbf{r})$, we calculate the velocity field $\mathbf{u}(\mathbf{r})$. We integrate the electron trajectories using a Runge-Kutta fourth-order method to represent the fluid streamlines, ensuring that the separation between streamlines is inversely proportional to the magnitude of the drift velocity. Last, we find the current density and numerically integrate its profile to compute the total current and the electrical resistance R . We give the resistance in units of the international system using $W = 1 \mu\text{m}$ and $W = 500 \text{ nm}$ for the elbow and the constriction geometries, and for graphene, with Fermi velocity $v_F = 10^6 \text{ ms}^{-1}$, at carrier density $n = 10^{12} \text{ cm}^{-2}$.

However, we can adapt it to other densities with a conversion factor.

We solve the Navier-Stokes equation using another finite element method and

$$\mathbf{u}(\mathbf{r}) = \sum_{n=1}^N \begin{pmatrix} u_{x,n} \\ u_{y,n} \end{pmatrix} \phi_n(\mathbf{r}), \quad V(\mathbf{r}) = \sum_{n=1}^N V_n \phi_n(\mathbf{r}). \quad (\text{B2})$$

Compared to the Boltzmann equation, the absence of an angular dependency in the Navier-Stokes model reduces its complexity. Therefore, we can accelerate calculations and better sample the geometry with smaller triangular elements. We now use $h < 0.1W$ for the elbow geometry and $h < 0.2W$ for the constriction, yielding $N \sim 2500$. We write the weak formulation for Eq. (5) and transform the continuous equations that govern the electronic flow into a solvable set of algebraic equations. We implement a partial slip boundary condition with the slip length given by Eq. (A4) at the device's edges. The velocity at the limits of the simulated cell is set by using the analytic solution of the velocity profile for a uniform channel [6].

For a set of physical parameters, γ_{ee} and γ_{mr} , we find the optimal elbow geometry by iteratively solving the Boltzmann equation for a set of points $\vec{G} = \{H_1, G_1, G_2\}$. We explore the set of values $0 < G_1, G_2 < 1.6W$ and H_1 in steps of size $0.2W$ and we identify the one with the lowest resistance R . For the optimal constriction, we explore the set of parameters $\vec{G} = \{G_1, G_2\}$, where $0 < G_1 < G_2 < W$ and we take steps of size $0.1W$. For the Navier-Stokes model, the triangular mesh is thinner, which enables us to explore the geometries in further detail, introducing more nodes to define the shape of the device. Particularly, we use $\vec{G} = \{H_1, \dots, H_5, G_1, \dots, G_5\}$ and $\vec{G} = \{G_1, \dots, G_4\}$ to characterize the elbow and the constriction, respectively. This number of points is enough to obtain a soft profile, and convergence is also achieved, since further increasing it does not significantly change the results. However, iteratively computing the resistance in such a parametric space is not feasible, so we use the MATLAB optimization algorithm, starting with a geometry in which $\vec{G} = \vec{0}$ and moving in the direction of the steepest descent in R to converge to the optimal geometry [58].

[1] G. Varnavides, A. Yacoby, C. Felser, and P. Narang, Charge transport and hydrodynamics in materials, *Nat. Rev. Mater.* **8**, 726 (2023).
 [2] M. Polini and A. K. Geim, Viscous electron fluids, *Phys. Today* **73**(6), 28 (2020).
 [3] B. N. Narozhny, Hydrodynamic approach to two-dimensional electron systems, *Riv. Nuovo Cim.* **45**, 1 (2022).
 [4] L. Fritz and T. Scaffidi, Hydrodynamic electronic transport, *Annu. Rev. Condens. Matter Phys.* **15**, 17 (2024).
 [5] G. Baker, M. Moravec, and A. P. Mackenzie, A perspective on non-local electronic transport in metals: Viscous, ballistic, and beyond, *Ann. Phys.* **536**, 2400087 (2024).
 [6] J. Estrada-Álvarez, F. Domínguez-Adame, and E. Díaz, Alternative routes to electron hydrodynamics, *Commun. Phys.* **7**, 138 (2024).

[7] X. Wang, P. Jia, R.-R. Du, L. N. Pfeiffer, K. W. Baldwin, and K. W. West, Hydrodynamic charge transport in an GaAs/AlGaAs ultrahigh-mobility two-dimensional electron gas, *Phys. Rev. B* **106**, L241302 (2022).
 [8] J. Gooth, F. Menges, N. Kumar, V. Süß, C. Shekhar, Y. Sun, U. Drechsler, R. Zierold, C. Felser, and B. Gotsmann, Thermal and electrical signatures of a hydrodynamic electron fluid in tungsten diphosphide, *Nat. Commun.* **9**, 4093 (2018).
 [9] A. Aharon-Steinberg, T. Völkl, A. Kaplan, A. K. Pariari, I. Roy, T. Holder, Y. Wolf, A. Y. Meltzer, Y. Myasoedov, M. E. Huber *et al.*, Direct observation of vortices in an electron fluid, *Nature (London)* **607**, 74 (2022).
 [10] Y. Wolf, A. Aharon-Steinberg, B. Yan, and T. Holder, Parahydrodynamics from weak surface scattering in ultraclean thin flakes, *Nat. Commun.* **14**, 2334 (2023).

- [11] J. Bernabeu and A. Cortijo, Bounds on phonon-mediated hydrodynamic transport in a type-I Weyl semimetal, *Phys. Rev. B* **107**, 235141 (2023).
- [12] P. J. Moll, P. Kushwaha, N. Nandi, B. Schmidt, and A. P. Mackenzie, Evidence for hydrodynamic electron flow in PdCoO₂, *Science* **351**, 1061 (2016).
- [13] Y. Wang, G. Varnavides, R. Sundararaman, P. Anikeeva, J. Gooth, C. Felser, and P. Narang, Generalized design principles for hydrodynamic electron transport in anisotropic metals, *Phys. Rev. Mater.* **6**, 083802 (2022).
- [14] A. C. Keser, D. Q. Wang, O. Klochan, D. Y. H. Ho, O. A. Tkachenko, V. A. Tkachenko, D. Culcer, S. Adam, I. Farrer, D. A. Ritchie *et al.*, Geometric control of universal hydrodynamic flow in a two-dimensional electron fluid, *Phys. Rev. X* **11**, 031030 (2021).
- [15] J. A. Sulpizio, L. Ella, A. Rozen, J. Birkbeck, D. J. Perello, D. Dutta, M. Ben-Shalom, T. Taniguchi, K. Watanabe, T. Holder, R. Queiroz, A. Principi, A. Stern, A. K. Scaffidi, T. Geim, and S. Ilani, Visualizing Poiseuille flow of hydrodynamic electrons, *Nature (London)* **576**, 75 (2019).
- [16] D. A. Bandurin, I. Torre, R. K. Kumar, M. Ben Shalom, A. Tomadin, A. Principi, G. H. Auton, E. Khestanova, K. S. Novoselov, I. V. Grigorieva, L. A. Ponomarenko, A. K. Geim, and M. Polini, Negative local resistance caused by viscous electron backflow in graphene, *Science* **351**, 1055 (2016).
- [17] D. A. Bandurin, A. V. Shytov, L. S. Levitov, R. K. Kumar, A. I. Berdyugin, M. Ben Shalom, I. V. Grigorieva, A. K. Geim, and G. Falkovich, Fluidity onset in graphene, *Nat. Commun.* **9**, 4533 (2018).
- [18] M. L. Palm, C. Ding, W. S. Huxter, T. Taniguchi, K. Watanabe, and C. L. Degen, Observation of current whirlpools in graphene at room temperature, *Science* **384**, 465 (2024).
- [19] K. G. Nazaryan and L. Levitov, Nonlocal conductivity, continued fractions, and current vortices in electron fluids, *Phys. Rev. B* **110**, 045147 (2024).
- [20] J. Estrada-Alvarez, E. Díaz, and F. Domínguez-Adame, Negative differential resistance of viscous electron flow in graphene, *2D Mater.* **12**, 015012 (2025).
- [21] P. Cosme and H. Terças, Hydrodynamical study of terahertz emission in magnetized graphene field-effect transistors, *Appl. Phys. Lett.* **118**, 131109 (2021).
- [22] J. H. Farrell, N. Grisouard, and T. Scaffidi, Terahertz radiation from the Dyakonov-Shur instability of hydrodynamic electrons in Corbino geometry, *Phys. Rev. B* **106**, 195432 (2022).
- [23] A. Hui, V. Oganessian, and E.-A. Kim, Beyond Ohm's law: Bernoulli effect and streaming in electron hydrodynamics, *Phys. Rev. B* **103**, 235152 (2021).
- [24] M. Kravtsov, A. Shilov, Y. Yang, T. Pryadilin, M. Kashchenko, O. Popova, M. Titova, D. Voropaev, Y. Wang, K. Shein *et al.*, Viscous terahertz photoconductivity of hydrodynamic electrons in graphene, *Nat. Nanotechnol.* **20**, 51 (2025).
- [25] D. Asafov, V. Kachorovskii, K. Tikhonov, and G. Zhang, Viscous flow through a finite-width slit: Boundary conditions and dissipation, *Phys. Rev. B* **106**, 224201 (2022).
- [26] S. S. Pershoguba, A. F. Young, and L. I. Glazman, Current distribution in a slit connecting two graphene half planes, *Phys. Rev. B* **102**, 125404 (2020).
- [27] R. Krishna Kumar, D. A. Bandurin, F. M. D. Pellegrino, Y. Cao, A. Principi, H. Guo, G. H. Auton, M. Ben Shalom, L. A. Ponomarenko, G. Falkovich, K. Watanabe, T. Taniguchi, I. V. Grigorieva, L. S. Levitov, M. Polini, and A. K. Geim, Superballistic flow of viscous electron fluid through graphene constrictions, *Nat. Phys.* **13**, 1182 (2017).
- [28] J. Estrada-Alvarez, J. Salvador-Sanchez, A. Pérez-Rodríguez, C. Sánchez-Sánchez, V. Clericò, D. Vaquero, K. Watanabe, T. Taniguchi, E. Diez, F. Domínguez-Adame, M. Amado, and E. Díaz, Superballistic conduction in hydrodynamic antidot graphene superlattices, *arXiv:2407.04527* [Phys. Rev. X (to be published)].
- [29] W. Huang, T. Paul, M. L. Perrin, and M. Calame, Eliminating the channel resistance in two-dimensional systems using viscous charge flow, *2D Mater.* **11**, 033001 (2024).
- [30] O. E. Raichev, Superballistic boundary conductance and hydrodynamic transport in microstructures, *Phys. Rev. B* **106**, 085302 (2022).
- [31] L. V. Ginzburg, C. Gold, M. P. Rössli, C. Reichl, M. Berl, W. Wegscheider, T. Ihn, and K. Ensslin, Superballistic electron flow through a point contact in a Ga[Al]As heterostructure, *Phys. Rev. Res.* **3**, 023033 (2021).
- [32] H. Guo, E. Ilseven, G. Falkovich, and L. S. Levitov, Higher-than-ballistic conduction of viscous electron flows, *Proc. Natl. Acad. Sci. USA* **114**, 3068 (2017).
- [33] P. S. Alekseev and M. A. Semina, Ballistic flow of two-dimensional interacting electrons, *Phys. Rev. B* **98**, 165412 (2018).
- [34] R. N. Gurzhi, Minimum of resistance in impurity-free conductors, *Sov. Phys. JETP* **17**, 521 (1963).
- [35] R. N. Gurzhi, Hydrodynamic effects in solids at low temperature, *Sov. Phys. Usp.* **11**, 255 (1968).
- [36] A. Stern, T. Scaffidi, O. Reuven, C. Kumar, J. Birkbeck, and S. Ilani, How electron hydrodynamics can eliminate the Landauer-Sharvin resistance, *Phys. Rev. Lett.* **129**, 157701 (2022).
- [37] W. Huang, T. Paul, K. Watanabe, T. Taniguchi, M. L. Perrin, and M. Calame, Electronic Poiseuille flow in hexagonal boron nitride encapsulated graphene field effect transistors, *Phys. Rev. Res.* **5**, 023075 (2023).
- [38] M. J. M. de Jong and L. W. Molenkamp, Hydrodynamic electron flow in high-mobility wires, *Phys. Rev. B* **51**, 13389 (1995).
- [39] R. Moessner, N. Morales-Durán, P. Surówka, and P. Witkowski, Boundary-condition and geometry engineering in electronic hydrodynamics, *Phys. Rev. B* **100**, 155115 (2019).
- [40] N. W. Ashcroft and N. D. Mermin, *Solid State Physics* (Thomson Learning, Boston, 1976).
- [41] M. Di Ventra, *Electrical Transport in Nanoscale Systems* (Cambridge University, Cambridge, 2008).
- [42] T. Holder, R. Queiroz, T. Scaffidi, N. Silberstein, A. Rozen, J. A. Sulpizio, L. Ella, S. Ilani, and A. Stern, Ballistic and hydrodynamic magnetotransport in narrow channels, *Phys. Rev. B* **100**, 245305 (2019).
- [43] K. Kapralov and D. Svintsov, Ballistic-to-hydrodynamic transition and collective modes for two-dimensional electron systems in magnetic field, *Phys. Rev. B* **106**, 115415 (2022).
- [44] P. S. Alekseev and A. P. Dmitriev, Hydrodynamic magnetotransport in two-dimensional electron systems with macroscopic obstacles, *Phys. Rev. B* **108**, 205413 (2023).
- [45] J. Callaway, Model for lattice thermal conductivity at low temperatures, *Phys. Rev.* **113**, 1046 (1959).
- [46] P. Ledwith, H. Guo, A. Shytov, and L. Levitov, Tomographic dynamics and scale-dependent viscosity in 2D electron systems, *Phys. Rev. Lett.* **123**, 116601 (2019).

- [47] P. S. Alekseev and A. P. Dmitriev, Viscosity of two-dimensional electrons, *Phys. Rev. B* **102**, 241409(R) (2020).
- [48] J. Hofmann and U. Gran, Anomalously long lifetimes in two-dimensional Fermi liquids, *Phys. Rev. B* **108**, L121401 (2023).
- [49] P. Alekseev, Viscous flow of two-component electron fluid in magnetic field, *Semiconductors* **57**, 193 (2023).
- [50] P. S. Alekseev, Negative magnetoresistance in viscous flow of two-dimensional electrons, *Phys. Rev. Lett.* **117**, 166601 (2016).
- [51] E. I. Kiselev and J. Schmalian, Boundary conditions of viscous electron flow, *Phys. Rev. B* **99**, 035430 (2019).
- [52] V. Clericò, J. A. Delgado Notario, M. Saiz-Bretín, A. V. Malyshev, Y. M. Meziani, P. Hidalgo, B. Méndez, M. Amado, F. Domínguez-Adame, and E. Diez, Quantum nanoconstrictions fabricated by cryo-etching in encapsulated graphene, *Sci. Rep.* **9**, 13572 (2019).
- [53] O. E. Raichev, Magneto-hydrodynamic boundary conditions for the two-dimensional fermion gas, *Phys. Rev. B* **108**, 125305 (2023).
- [54] P. G. Ciarlet, *The Finite Element Method for Elliptic Problems* (SIAM, Philadelphia, 2002).
- [55] D. Engwirda and D. Ivers, Off-centre Steiner points for Delaunay-refinement on curved surfaces, *Comput.-Aided Design* **72**, 157 (2016).
- [56] P. Jiang, Y. Zhang, Q. Zhou *et al.*, An adaptive sampling strategy for Kriging metamodel based on Delaunay triangulation and TOPSIS, *Appl. Intell.* **48**, 1644 (2018).
- [57] D. J. Mavriplis, An advancing front Delaunay triangulation algorithm designed for robustness, *J. Comput. Phys.* **117**, 90 (1995).
- [58] J. C. Lagarias, J. A. Reeds, M. H. Wright, and P. E. Wright, Convergence properties of the Nelder-Mead simplex method in low dimensions, *SIAM J. Optim.* **9**, 112 (1998).